Rivero, A. E., Fournier, S. F. B., Manolesos, M., Cooper, J. E., & Woods, B. K. S. (2020). Wind Tunnel Comparison of Flapped and FishBAC Camber Variation for Lift Control. In *AIAA Scitech 2020 Forum* [AIAA 2020-1300] American Institute of Aeronautics and Astronautics Inc. (AIAA). https://doi.org/10.2514/6.2020-1300

Peer reviewed version

Link to published version (if available):
10.2514/6.2020-1300

Link to publication record in Explore Bristol Research
PDF-document

University of Bristol - Explore Bristol Research
General rights

Wind Tunnel Comparison of Flapped and FishBAC Camber Variation for Lift Control

Andres E. Rivero* and Stephane Fournier[†]
Bristol Composites Institute (ACCIS), University of Bristol, Bristol, BS8 1TR, UK

Marinos Manolesos[‡]
College of Engineering, Swansea University, Bay Campus, Swansea, SA1 8EN, UK

Jonathan E. Cooper[§]
Department of Aerospace Engineering, University of Bristol, Bristol, BS8 1TR, UK

Benjamin K. S. Woods[¶]
Bristol Composites Institute (ACCIS), University of Bristol, Bristol, BS8 1TR, UK

Unlike hinged flaps (e.g. ailerons, elevator and rudder), camber morphing devices vary camber distribution in a smooth and continuous way, resulting on aerodynamic efficiency improvements due to the absence of surface discontinuities. One such camber morphing concept, the Fish Bone Active Camber (FishBAC) device, has shown significant aerodynamic benefits when compared to a flap. A 2D wind tunnel test was performed to further investigate the FishBAC's behavior in terms of its aerodynamic performance and the size and structure of the shed wake. To establish a direct comparison, a hinged flap was also tested under equivalent flow conditions. A combination of quasi-steady force balance and wake rake pressure measurements were used to determine aerodynamic force coefficients. Additionally, these measurements are complemented by a flow visualization study performed using Particle Image Velocimetry, where a visual comparison on the size and vortical structure of the near field wakes was conducted. Results show that the FishBAC achieves at least 16% higher aerodynamic efficiency than the flap.

I. Nomenclature

α_u	=	uncorrected angle of attack
α	=	corrected angle of attack
c	=	chord length
c_d	=	corrected drag coefficient
c_{d_u}	=	uncorrected drag coefficient
C_{d_0}	=	profile drag coefficient
c_l	=	corrected lift coefficient
c_{l_u}	=	uncorrected lift coefficient
c_{m_u}	=	uncorrected moment coefficient at quarter-chord
C	=	wind tunnels cross-sectional area
da	=	differential area perpendicular to wake
D	=	drag force
δ	=	actuation input angle
ϵ_{sb}	=	solid blockage correction factor
ϵ_{wb}	=	wake blockage correction factor
F_{i_1}	=	bottom balance measured force
F_{i_2}	=	top balance measured force
H	=	total pressure
L	=	lift force
p	=	static pressure

---
*PhD Student, Bristol Composites Institute (ACCIS), Department of Aerospace Engineering. AIAA Student Member.

[†]Senior Research Associate, Bristol Composites Institute (ACCIS). AIAA Member.

[‡]Senior Lecturer in Aerospace Engineering, College of Engineering, Swansea University. AIAA Member.

[§]RAEng Airbus Sir George White Professor, Department of Aerospace Engineering. AIAA Fellow.

[¶]Lecturer in Aerospace Structures, Bristol Composites Institute (ACCIS). AIAA Member.

q	=	dynamic pressure
ρ	=	air density
Re_u	=	uncorrected Reynolds number
Re	=	corrected Reynolds number
S	=	wing planform area
V_{model}	=	wing volume
V_0	=	freestream flow speed
σ	=	non-dimensional wing-to-tunnel geometric relationship

II. Introduction

Modern fixed-wing aircraft are maneuvered by control surfaces that vary airfoil camber. These variations in camber create time varying forces and moments that allow to control the airplane. Traditionally, these changes in camber are achieved by actuating a series of hinged flaps that are located at trailing edge of the airfoil. Depending on their location, these flaps are known as ailerons, elevator and rudder. Although simple, effective, and ubiquitous, the sudden and discontinuous camber change created by flaps causes a significant increase in drag.

An alternative to hinged flaps is camber morphing, which change camber in a smooth and continuous way, without sharp surface discontinuities, and without the chordwise gaps typically present between the flap and the rest of the wing. These devices can produce similar changes in lift coefficient as hinged flaps, but with a much lower drag penalty [1]. Consequently, they have been a subject of a significant amount of research over the past decades, as reviewed by Barbarino et al. [2]. With reduction of the inherent drag penalty of hinged flaps comes a promising set of opportunities to use camber morphing (beyond control purposes) to continuously optimize performance throughout flight. These improvements in performance can be both in a two-dimensional sense, by optimizing the lift-to-drag ratio of the airfoil at any flight stage, and in a three-dimensional sense through spanwise variation of camber to optimize the spanwise lift distribution to reduce induced drag [3].

Although not a new concept—indeed camber morphing mechanisms date from as early as 1920 [4–6]—interest in these concepts has resurged in the past two decades due to advancements in smart materials and lightweight composite structures. For example, the use piezoelectric actuators [7, 8], shape memory alloy [9, 10] and composite bistable laminates [11, 12] have shown successful ways to achieve the required shape change capabilities.

In terms of camber morphing prototypes found in the literature, some of the highlighted concepts are the F-111 Mission Adaptive Wing, based on a series of several hinged flaps [13]; the Flexys Flexfoil, capable of achieving ±10° of out-of-plane deflection; DARPA Smart Wing, which combined a plate structure with a honeycomb core [14]; the DLR Belt-Rib concept [15] and the Fish Bone Active Camber (FishBAC) morphing trailing edge device, which is subject of study of this wind tunnel experiment (Fig. 1) [16].

However, it can be observed in the literature that these camber morphing studies that most of the research efforts have focused on the structural design and analysis. Aerodynamic comparisons between these devices and traditional hinged control surfaces–specifically wind tunnel data—are scarce. Early studies in late 1980s and early 1990s introduced preliminary results that show, quantitatively, and improved of aerodynamic efficiency of up to 9% when variable camber morphing is used. However, these results are not related to a specific morphing concept [15, 17, 18]. Another preliminary study based on wind tunnel data even predicts a 3 to 6 percent reduction in fuel consumption, for a long/medium range civilian aircraft [1].

Daynes and Weaver [19] carried out a wind tunnel test of a compliant trailing edge, where an increase of lift coefficient of $\Delta C_L \approx 0.5$ can be observed when actuating the morphing device between ±10° deflection. No flap comparison was performed in this study. Bilgen et al. [20] also conducted a 2D wind tunnel test comparison of a flapped airfoil versus a Macro-Fibre-Composite (MFC) actuated variable camber wing and results showed higher lift-to-drag ratios of 10%-50% for the camber morphing wing.
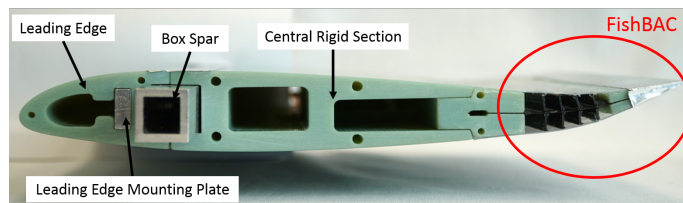

Fig. 1 FishBAC camber morphing trailing edge device attached to a NACA 23012 wing tunnel model.

Ai et al. [21] also presented a wind tunnel test comparison—validated agains Computational Fluid Dynamics (CFD) analysis—of several camber morphing cases versus a hinged flap. Although they showed improvements in aerodynamic efficiency, these improvements were limited to low angles of attack, achieving an increase in L/D of about 9% at zero-degree angle of attack. Moreover, Yokozeki et al. [22] presented wind tunnel test results for a corrugated camber morphing device. These results do not show significant improvement in aerodynamic efficiency when compared to a flap. However, it is important to note that this particular morphing device presents a smooth skin on the top surface only, leaving the core corrugations exposed on the bottom surface, which likely added drag to the camber morphing device.

The subject of this study, the Fish Bone Active Camber (FishBAC) concept, was originally introduced by Woods and Friswell [16]. The FishBAC is a morphing trailing edge device that is capable of generating large, smooth and continuous changes in camber distribution. It benefits from an anisotropic design, being significantly more compliant chordwise than spanwise. This anisotropic nature reduces the actuation energy requirements needed to achieve large chordwise deflections, while still being rigid enough to resist spanwise bending moments. In terms of structural configuration, the FishBAC consists of a central bending plate (spine), a series of spanwise stringers, an elastomeric pre-stressed skin and a series of antagonistic tendons that transfer actuation torque input into the bending spine by using spooling pulleys.

A preliminary wind tunnel test of the FishBAC [23] showed a potential improvement in lift-to-drag ratio between 20 and 25 percent, compared to a 25% chord trailing edge flap. It also showed a FishBAC lift control authority of $\Delta C_L \approx 0.72$. However, the authors discussed the presence of 3D effects due to the nature of their wind tunnel setup that may have affected the results quality. Additionally, the FishBAC concept has evolved since that initial wind tunnel test: the morphing section is now localized, approximately between $0.75c$ and $0.9c$ of chord, instead of between $0.35c$ and $0.85c$. Therefore, additional wind tunnel tests should be performed to further investigate the aerodynamic behavior of the FishBAC using the most recent configuration.

The objective of this wind tunnel experiment is to reassess the benefits of the FishBAC, experimentally, using an improved design of FishBAC installed into a longer span wing and tested in closed return and closed test section tunnel for improved flow quality. Furthermore, the instrumentation used to quantify the performance is significantly improved from the preliminary wind tunnel test by Woods et al. [23], as force balances and a pressure-based wake rake are used for more reliable aerodynamic forces measurements. Also, this experiment addresses the lack of flow visualization studies of camber morphing devices in the literature by performing flow visualization measurements using Particle Image Velocimetry (PIV). These measurements not only be used to enhance the understanding of the benefits of camber morphing by studying the changes in wake patterns and comparing them to the wake of a hinged flap, but also provide insight into the coupled aeroelastic response of the system that is useful for design improvements and for future validation of fluid-structure interaction (FSI) analysis.

This paper is structured as follows: first, an introduction of the test methodology and test cases are presented, followed by a summary of the wind tunnel data corrections, and presentation of the aerodynamic coefficients, lift-curve slopes and optical measurements (PIV). Finally, the conclusions summarize the major findings of this study.

III. Methodology

This section introduces the wind tunnel testing methodology, including details of the tunnel itself, the equipment and instrumentation used, and the configurations tested.

A. Wind Tunnel & Equipment

The Swansea University closed return low speed wind tunnel with a 1.5 m wide x 1 m tall closed test section was used for this experiment (Fig. 2). This tunnel has a maximum freestream velocity of 50 m/s, and flow characterization studies have measured turbulence intensity, velocity uniformity and flow angularity values of 0.175%, 0.04% and ±0.1°, respectively. A turntable with movable range of ±90° and accuracy of ±0.05° controls the angle of attack of the wing. Furthermore, the wing was mounted vertically in the test section and was attached to two strain-gauge based AMTI MC12-1000 six-axis force balances, one on each end. Equipped with a temperature control system, a target temperature of 20 °C is maintained within ±2° accuracy. A closed loop feedback system controls wind speed using real time velocity calculations based on a precision differential pressure sensor with a range of ±2500 Pa [24], which measures the pressure difference at the contraction section upstream of the test section.

1. Pressure Wake Rake

A pressure-based wake rake for wake survey (Fig. 3) has recently been added to the Swansea Low-Speed Wind Tunnel. The rake consists of 60 total pressure and 3 static pressure tubes mounted 4.5 chords downstream of the wing trailing edge. This mounting distance allows for pressure recovery in the wake. The total and static pressure tubes, respectively, are aligned in the thicknesswise direction (which is horizontal with a vertical wing mounting), with a spanwise offset between the total and static pressure tubes to avoid interference. A *Scanivalve* MPS4264 miniature pressure scanner is connected to the rake tubes and measures the total pressure at each tube, individually. The total pressure tubes have variable thicknesswise spacing of between 3.9 mm (at center) and 15.9 mm (toward the ends), covering a total thicknesswise width of 500 mm. This variable spacing allows to perform more pressure measurements in the wake region than outside the wake, improving the overall accuracy of the drag measurements.
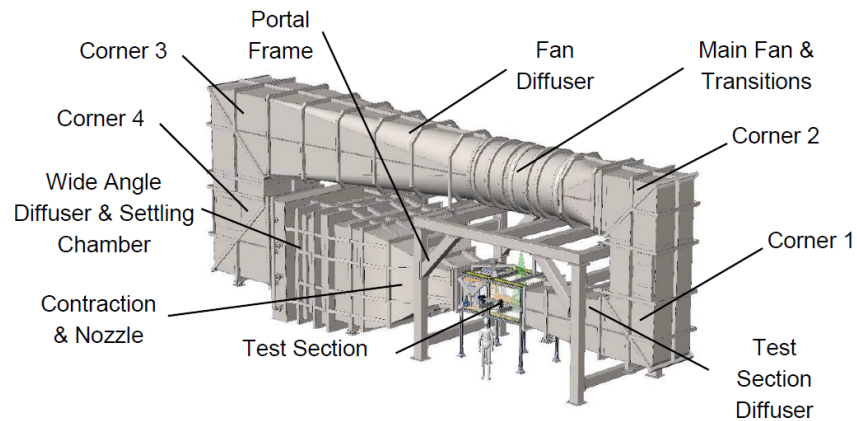

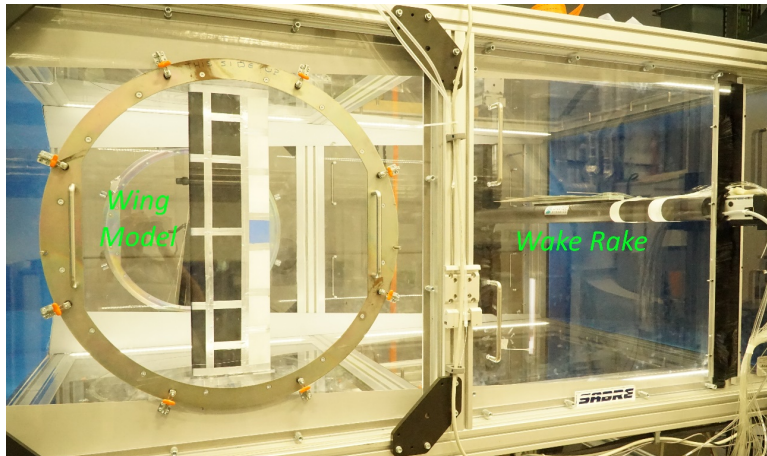**Fig. 2   3D rendering of Swansea University's Low Speed Wind Tunnel.**

Fig. 3   Wind tunnel test section with pressure-based wake survey system at Swansea University's Low Speed Wind Tunnel.

2. Image Measurements: Particle Image Velocimetry

An external *LaVision®* Particle Image Velocimetry system is used for aerodynamic image measurements, controlled with the DaVis 10 software platform. An sCMOS 5.5-megapixel double shutter camera is located at the trailing edge of the wing and is used to measure the wake of both FishBAC and flap in a quasi-static flow condition. This camera can take two images within 120 ns, making them suitable for PIV applications. Additionally, the camera has an exposure time range between 15 μs and 100 ms and a frame rate of 50 fps. A particle generator was used to generate seeding particles with an average diameter of 1 μm. Lastly, a dual cavity, double pulse 200 mJ Nd:YAG green laser with a wavelength of 532 nm was used to illuminate the measuring plane. Fig. 4 shows a schematic of the PIV setup.
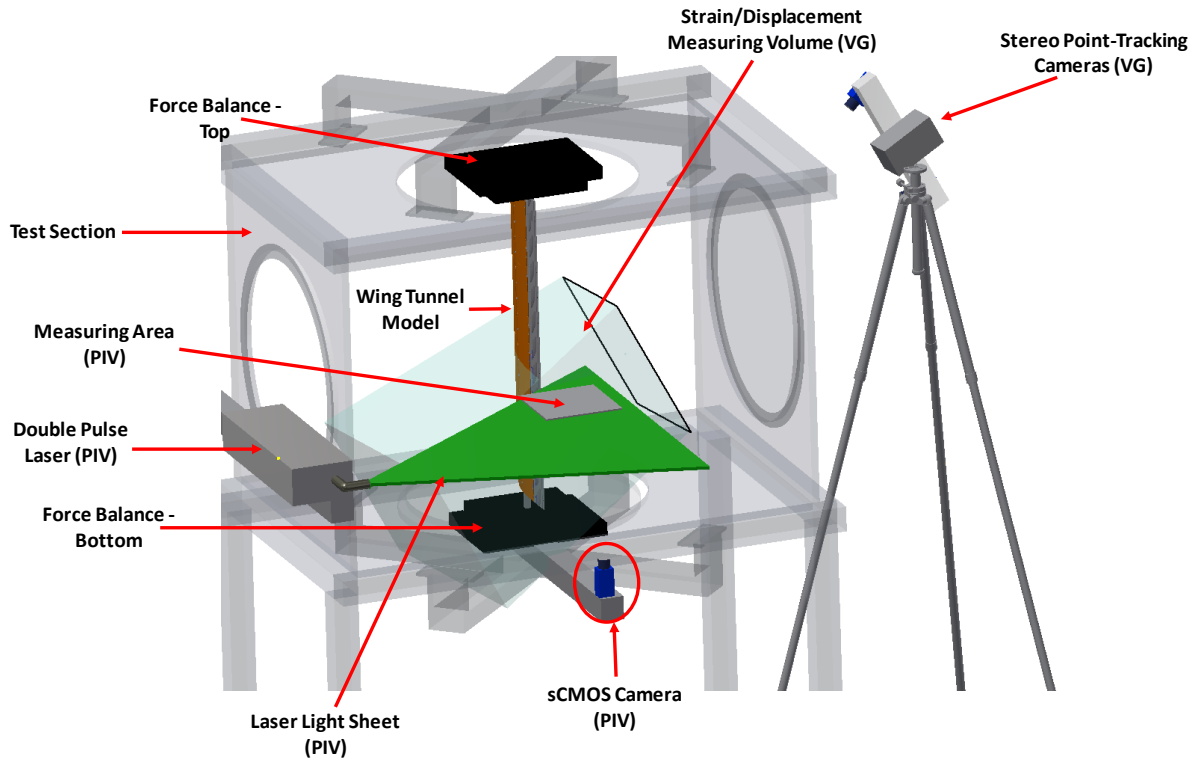

Fig. 4   Schematic of the wind tunnel test setup, including wind tunnel wing model, force balances and PIV equipment.

B. Wind Tunnel Wing Model

A two-dimensional wind tunnel model of a NACA 23012 airfoil was designed and manufactured for this wind tunnel experiment. The wing spans the 1-meter height of the test section (Fig. 3) and has a chord length of 270 mm. The wing has two main sections: a front rigid section that starts at the leading edge and ends at 75% of the chord, and a trailing edge section. The front rigid section is composed of 3D-printed plastic leading edge and center sections that are bolted to an aluminum (6082T alloy) box spar located at the quarter chord. Three interchangeable 'cartridge-like' trailing edge sections were created to allow testing of the baseline NACA 23012, a 25% trailing edge flap version, and a 25% trailing edge FishBAC. The aluminum spar is clamped in one end to the bottom force balance, which rotates with the turntable. Since the top force balance does not rotate, the other side of the spar connects to it via a spherical bearing to allow for angle of attack rotation and to minimize the bending moments reacting into the upper balance. Details of the construction of the three configurations follow:

1) Rigid NACA 23012 Airfoil

A 3D printed rigid NACA 23012 trailing edge section is tested to obtain a baseline data set, used to acquire lift and drag properties of this airfoil section when no changes of camber occur. Results from the baseline airfoil will be used to validate the tunnel instrumentation, before being used as a reference against which the flap and FishBAC will be compared.

2) Trailing Edge Flap

A 3D-printed hinged flap of the same chord dimension of the FishBAC is tested to directly compare the two approaches. The flap is mounted to a steel shaft and actuated by two KST X10 high voltage servos that are connected to the flap by a system of two external control horns and linkage bars. The flap is a plain flap, with no aerodynamic overhang (which is sometimes used to reduce hinge moments at the expense of added drag) and with the minimal realizable gap between the flap and the rigid wing section, on the order of 2 mm. The flap has an unloaded deflection range of $\pm 30°$.

3) Camber Morphing: FishBAC

The central bending spine of the FishBAC (Fig. 5) was manufactured using three plies of 8552/IM7 carbon fibre prepreg, with a total cured thickness of 0.39 mm. A stacking sequence of $[90/0/90]_T$ (with 90 degrees being the spanwise direction) was used to provide additional material anisotropy to complement the geometric anisotropy of the FishBAC. A total of eight stringers (four on each surface) were 3D-printed along with a solid trailing edge insert and then bonded to the spine using a cyanoacrylate adhesive. Moreover, the FishBAC is actuated at two spanwise points located between $[0.07b, 0.095b]$ and $[0.93b, 0.955b]$, respectively. Each actuation point is fitted with two KST X10 high voltage servo actuators with a maximum output torque of 1.05 N. The torque is transmitted from the actuators to the composite spine using an antagonistic tendon system. The 25 mm wide aramid fibre (Kevlar) tape was run through slots in the stringers and over the trailing edge insert before being stitched and bonded to the trailing edge of the carbon spine. Transverse deflections of up to $\pm$ 10% chord can be achieved when actuated in absence of aerodynamic loads. It is worth noting here that the use of two fairly spaced out actuation points along the span will lead to variations in camber along the span due to elastic washout, introducing 3D effects to the wind tunnel test. In this particular specimen, the use of printed plastic stringers instead of composite ones significantly reduces the spanwise rigidity, exacerbating washout.
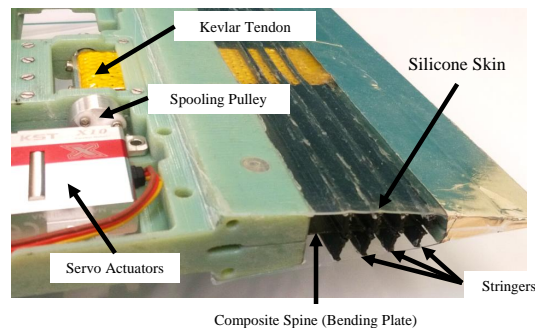

Fig. 5   FishBAC structure and actuation mechanism.

C. Aerodynamic Predictions: XFOIL

To compare wind tunnel test baseline results, two-dimensional numerical predictions of the aerodynamic performance of the baseline airfoil were obtained using the XFOIL panel method software [25]. Reynolds and Mach number were set to 543,000 and 0.087 respectively to match the experimental values. Additionally, to roughly match the turbulence intensity of the Swansea Wind Tunnel, a value of N_{crit} equal to 5 was used for all XFOIL estimates.

IV. Test Cases

For the three wing configurations, experiments were run at a freestream velocity of 30 m/s and a temperature of 20 °C, which corresponding to a Reynolds number of about 540,000. The angle of attack was varied from $\alpha = -5°$ to $\alpha = +14°$, in increments of $\alpha = 1°$. Force balance data was recorded for 30 s for each test condition at a sampling rate of 300 Hz, and then time averaged to give quasi-steady results. The same data recording process was followed for wake survey, which was synchronized with balance measurements using a sampling time and rate of 20 s and 10 Hz, respectively. Two types of wake rake measurements were performed: *(i)* actuation and angle of attack sweeps with the wake rake at a fixed spanwise location, and *(ii)* spanwise wake rake location sweeps at fixed angle of attack and actuation input. These two types of measurements allow drag to be quantified as a function of both angle of attack and spanwise location. A summary of test cases can be found in Table 1.

V. Data Processing

The following section outlines the data analysis process, including equations used to process balance and wake rake data, the wind tunnel corrections for three-dimensional effects and post-processing parameters the PIV system.

A. Force Balance Data

Aerodynamic forces and moments were measured by the two force balances, individually, and then combined to calculate the total resultant forces and moments. Each balance measures in its own respective coordinate frame. Since the bottom balance rotates with the turntable while the top balance is fixed, the forces measured by the bottom balance need to be converted to the global coordinate frame. Hence, the total lift force is calculated by

$$L = F_{y_1} cos(\alpha_u) - F_{x_1} cos(\alpha_u) - F_{y_2} \quad \text{and} \quad D = F_{x_1} cos(\alpha_u) + F_{y_1} cos(\alpha_u) + F_{x_2} , \tag{1}$$

where F_{x_1} and F_{y_1} correspond to the bottom balance and F_{x_2} and F_{y_2} correspond to the top balance. Furthermore, zero wind speed tare measurements were recorded before and after each angle of attack sweep. These were later subtracted from the force balance data set to account for any offsets or time drift in the measured values. Once the total lift and drag forces were calculated, the non-dimensional lift and drag coefficients were estimated by normalizing the total forces by the dynamic pressure and the wing planform area, such that

$$C_{L_u} = \frac{2L}{\rho V_\infty^2 S} \quad \text{and} \quad C_{D_u} = \frac{2D}{\rho V_\infty^2 S} . \tag{2}$$

Since accurate two dimensional drag measurements from balance setups such as the one used can be difficult (due in part to the large differences between lift and drag forces, the range of the load cells used, and the presence of end gaps and wall effects) wake survey measurements were used to give more accurate two dimensional measurements of drag using wake momentum deficit [26].

Table 1 Wind tunnel test configurations and test cases.

Configuration	Actuation Input Angle	PIV
Baseline	N/A	No
Flap	$\delta = [-20°, +30°]$, $\Delta\delta = +10°$	Yes
FishBAC	$\delta = [+0°, +40°]$, $\Delta\delta = +10°$	Yes

B. Wake Rake Data

Drag can be measured by comparing the momentum of the air in the freestream against that measured in the flow behind the model. This method assumes that the wind tunnel walls are parallel and with negligible shear stresses. This theory is based on the assumption that, as the flow passes over a wind tunnel model, it suffers a loss of momentum that is equal to the profile drag of the body [26], such that

$$D = \dot{m}\Delta V = \iint (\rho V)(V - V_0)da \ , \tag{3}$$

where V_0 is the freestream velocity, V is the final flow speed in the wake and da is the differential area perpendicular to the airstream at the wake. If normalized by the dynamic pressure, the profile drag coefficient can be obtained using the expression

$$C_{d0} = 2 \iint \left(\frac{V}{V_0} - \frac{V^2}{V_0^2} \right) \frac{da}{S} \ . \tag{4}$$

Combined with Bernoulli's equation, Eq. (4) can be derived in terms of total and static pressures, such that

$$C_{d0} = 2 \int \left(\sqrt{\frac{H - p}{H_0 - p_0}} - \frac{H - p}{H_0 - p_0} \right) \frac{dy}{c} = 2 \int \left(\sqrt{\frac{q}{q_0}} - \frac{q}{q_0} \right) \frac{dy}{c} \ , \tag{5}$$

where H, p and q are the total, static and dynamic pressures at the wake, respectively, and H_0, p_0 and q_0 are the same pressure quantities in the freesteam. Fig. 6 shows a schematic of the wake deficit of a wing inside a wind tunnel.
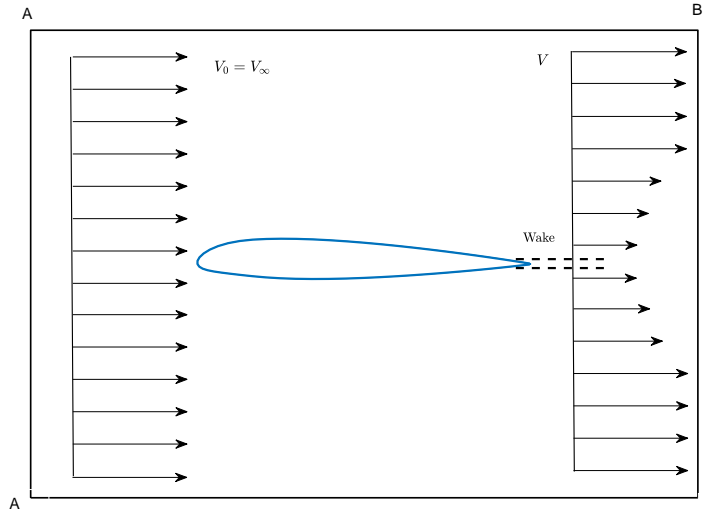

Fig. 6   Wind tunnel model's downstream wake.

An example of typical wake survey data are shown in Fig. 7. The pressure distribution at the wake along the thicknesswise direction allows to identify its behavior with increasing angle of attack. It is observed that the size of the wake grows in thickness and the pressure drop is more significant as angle of attack increases, resulting in higher drag. Also, the center of the wake shifts downward due to both the increase in angle of attack and circulation. Note that drag calculations using wake pressure are strictly valid for attached flow cases only, and therefore, measurements after stall angle were also ignored. Additionally, unsteady pressure data cases were also ignored based on the flow steadiness levels determined by the standard deviation of each set of pressure measurements.
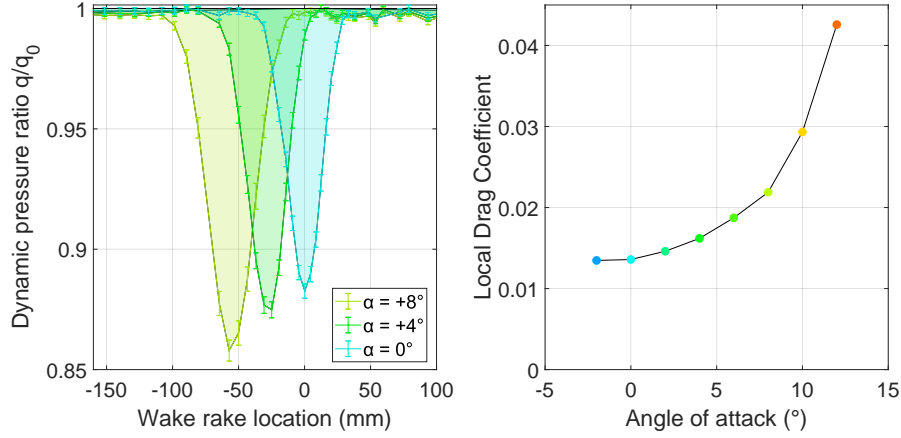
Fig. 7 FishBAC's wake survey data at half-span and actuator deflection input $\delta = +40°$: ratio between dynamic pressure in the wake and free stream at several angle of attacks (left) and profile drag coefficient vs α (right).

C. Wind Tunnel Corrections

To correct for three-dimensional effects, wind tunnel corrections are applied to account for solid and wake blockage and streamline curvature. The correction factors implemented in this study are the standard ones given by Barlow et al. [26]. Solid blockage occurs due to two main factors: *(i)* the reduction of the area through which the air flows caused by the presence of the wind tunnel model and *(ii)* the constraint of the tunnel walls, which increases the velocity of the air around the model. This correction factor is a constant value that does not change throughout the experiment and it is defined as

$$\epsilon_{\text{sb}} = \frac{K_1 V_{\text{model}}}{C^{1.5}} \; , \tag{6}$$

where V_{model} corresponds to 70% of the wing tunnel model volume, K_1 is approximately equal to 0.52 for wind tunnel models that span the tunnel's height and C is equal to the test sections cross-sectional area [26].

The second correction factor is for wake blockage, which occurs due to the air flow being restricted by the presence of the wake behind the model. This correction factor varies during the experiment as it depends on the size of the wake, which is directly proportional to the drag coefficient. This correction factor is defined as

$$\epsilon_{\text{wb}} = \frac{c/h}{2} C_{d_u} \; , \tag{7}$$

where h corresponds to the wind tunnel height and c correspond to the height of the wind tunnels test section. Moreover, the existence of streamline curvature due to wind tunnel walls is corrected using a geometric non-dimensional factor that relates the size of the wind tunnel model and the test section. It is defined as

$$\sigma = \frac{\pi^2}{48} \left(\frac{c}{h}\right)^2 \; . \tag{8}$$

These factors are then used to correct the lift (Eq. (9a)) and drag (Eq. (9b)) coefficients, as well as the angle of attack (Eq. (9c)) and Reynolds number (Eq. (9d)). These corrected expressions are defined as:

$$C_l = C_{l_u}[1 - \sigma - 2(\epsilon_{\text{sb}} + \epsilon_{wb})] \, , \tag{9a}$$

$$C_d = C_{d_u}(1 - 3\epsilon_{\text{sb}} - 2\epsilon_{\text{wb}}) \, , \tag{9b}$$

$$\alpha = \alpha_u + \frac{57.3}{2\pi}(C_{l_u} + 4C_{m_u}) \, , \tag{9c}$$

$$Re = Re_u[1 + (\epsilon_{\text{sb}} + \epsilon_{\text{wb}})] \; . \tag{9d}$$

9

D. Particle Image Velocimetry

Two-dimensional PIV measurements were performed to measure the flow velocity in a portion of the near field wake of both FishBAC and flap configurations. A $200\,\text{mm} \times 200\,\text{mm}$ calibration plate was used to define the measuring area, which was placed at a spanwise location of $0.467b$ (i.e. just below the midspan). This location is well outside the wind tunnel wall-effect regions, hence, the wake measurements are representative of two-dimensional flow. All PIV measurements were performed at a fixed angle of attack equal to $\alpha = 5°$ to ensure attached flow. To compare the impact of camber deflection on wake size and velocity for both the morphing and hinged trailing edge devices, a total of four FishBAC and flap deflections were sampled.

For each configuration, a total of 1000 images were taken at a frequency of 10 Hz, with a differential time of $dt = 13.5\,\mu s$ between the two laser pulses. To filter noise, a minimum image intensity was calculated for each data set, and then subtracted from all images in that set. Post-processing of images was performed using LaVision® DaVis 10 software. An interrogation area of 48 pixels was chosen (equivalent to 3.6 mm in both directions), as suggested by DaVis 10 for a flow velocity of 30 m/s. Finally, the time-average of each velocity field data set was calculated, resulting in a single time-average image per configuration.

VI. Results

The following section introduces the wind tunnel test results. These include a comparison between the aerodynamic behavior of the FishBAC and the flap using both balance data and pressure-based wake survey measurements. Finally, PIV results are also shown.

A. Aerodynamic Forces

This subsection directly compares the NACA 23012 rigid airfoil configuration described in Section III.B with previous experimental data from the literature and 2D XFOIL predictions. Fig. 8 shows both experimental and predicted lift and drag curves. The experimental data was obtained from Ashenden et al. [27] and Pouryoussefi et al. [28], which both tested at similar Reynolds numbers ($Re = 550000$ and $Re = 600000$, respectively). However, it is important to note that these two experiments used pressure taps on the surface to obtain both lift and drag. Hence, some discrepancies are expected due to differences in measuring techniques.

Fig. 8 shows that the lift curve measured in this work is similar to Pouryoussefi et al.'s results [28], whereas Ashenden et al. [27] has a similar behaviour to XFOIL. The reduction in measured lift performance could be due to the different measuring techniques: Ashenden et al. measured local section lift coefficient using pressure taps, whereas the presented results correspond to the average total lift as measured by the force balances. Additionally, Leishman [29] and Jacobs and Sherman [30] show NACA 23012 experimental maximum lift coefficients for similar Reynolds Number. Both results show a maximum lift coefficient estimates of $C_{L_{\max}} \approx 1.25$, which is closer to the $C_{L_{\max}} \approx 1.14$ obtained in this experiment and suggests that XFOIL may over-predict maximum lift coefficient. Lastly, it is important to point out that the results suggest the existence of an angle of attack misalignment on the presented wing model setup, as the lift coefficient at $\alpha = 0°$ is close to zero, which does not correspond to a cambered airfoil (Fig. 8).

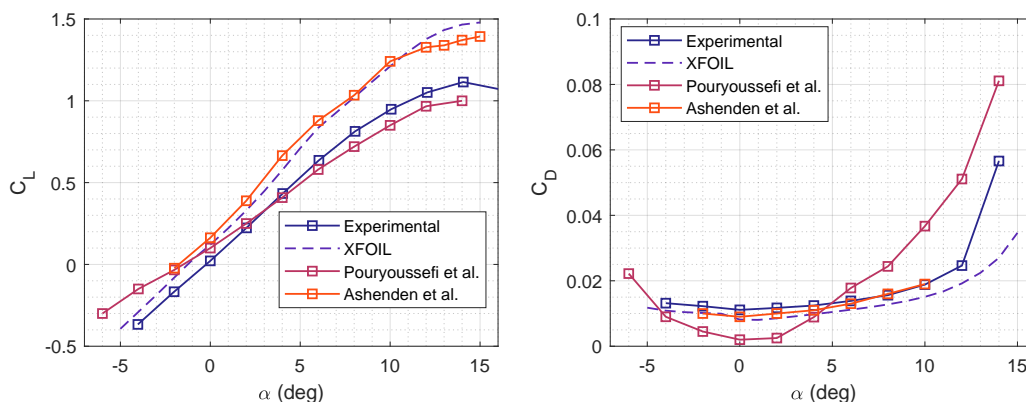**Fig. 8   NACA 23012 rigid configuration experimental lift and drag curves vs 2D panel method results (XFOIL).**

10

When analyzing the drag coefficient results in Fig. 8, it is observed that the obtained experimental results (wake rake) are similar to those obtained by Ashenden et al. [27]. Unlike lift coefficient, drag coefficient was calculated using local section wake rake data instead of average forces (force balance). This difference in measuring technique is a likely explanation of the better agreement between the currently measured drag results with Ashenden et al.'s results, as opposed to the existing discrepancies between the lift curves.

In summary, the NACA 23012 baseline results agree reasonably well with previous experimental and XFOIL measurements. However, it is observed that the obtained results have lower lift coefficients than those presented in the literature and the ones obtained with XFOIL. One potential reason for this is the 'modularity' of the wind tunnel wing model, which presents gaps that are covered with aluminum tape. Surface quality is very important at low Reynolds number and can reduce performance. Also, it is worth noting that the primary aim of this study is to compare the FishBAC to the flap, and so the relative (as opposed to absolute) aerodynamic performance is of key importance, and any issues caused by the construction of the model are present in both.

1. FishBAC vs. Flap

A comparison between measured lift and drag coefficients for the FishBAC and flap are shown in Figs. 9 and 10, respectively. It is observed in these figures that deflecting both the FishBAC and flap has a similar impact on the lift curves. As expected, increasing camber 'moves' the lift curve up an to the left, increasing lift at a given angle of attack, but also lowering the angle at which stall occurs.

In terms of lift control authority, the FishBAC and flap show an overall $\Delta C_L \approx 0.55$ and $\Delta C_L \approx 0.57$, respectively—considering trailing edge down deflections only. It is also observed that the amount of extra lift (ΔC_L) that it is generated for each each deflection increment diminishes. This behavior was also observed in previous FishBAC studies and was attributed to pressure losses due to flow separation with increasing camber [31].

While the FishBAC and flap both have a very large lift control authority, comparison of the associated drag coefficients in Figs. 9-10 shows that the flap configuration incurs a much higher drag penalty. This drag increase ranges from 74% to 80% for the $\delta = +10$ and $\delta = +30$ configurations, respectively (Fig. 10). To directly compare aerodynamic efficiency, lift-to-drag ratios as a function of both angle of attack and lift coefficient are presented in Figs. 11 and 12 for FishBAC and flap, respectively. It is observed that, for a given deflection, the FishBAC presents a higher efficiency that ranges between 22% and 83% increase, depending on the input angle.
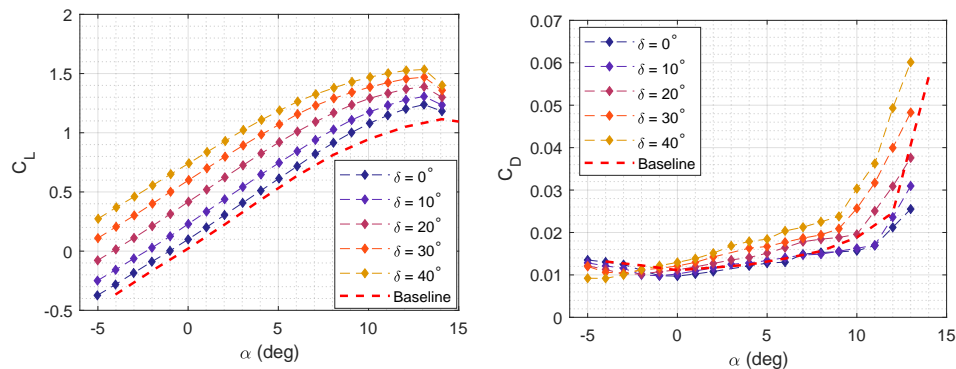

Fig. 9   FishBAC lift and drag coefficients as a function of angle of attack at various actuation input angles.
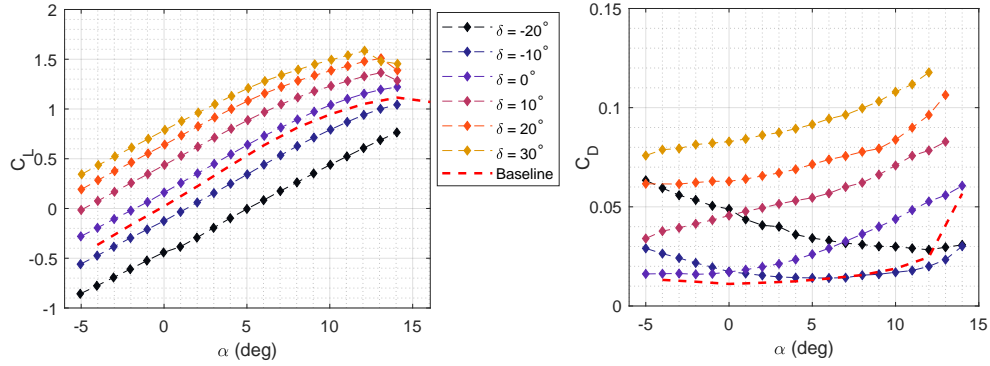
Fig. 10   Flap lift and drag coefficients as a function of angle of attack at various actuation input angles.
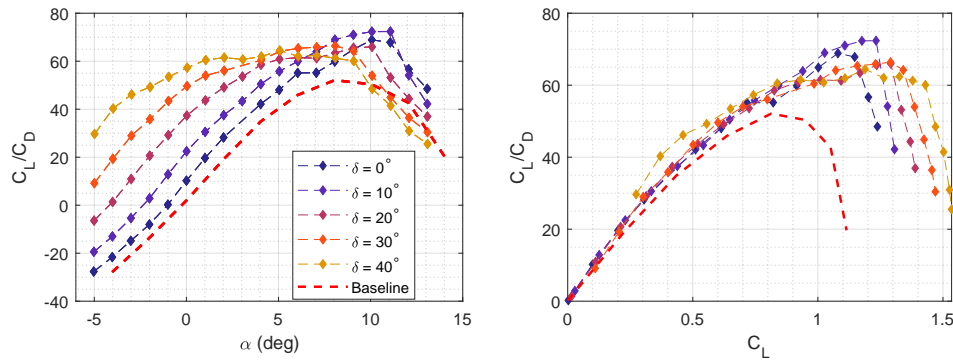

Fig. 11   FishBAC aerodynamic efficiency as a function of both angle of attack and lift coefficient.
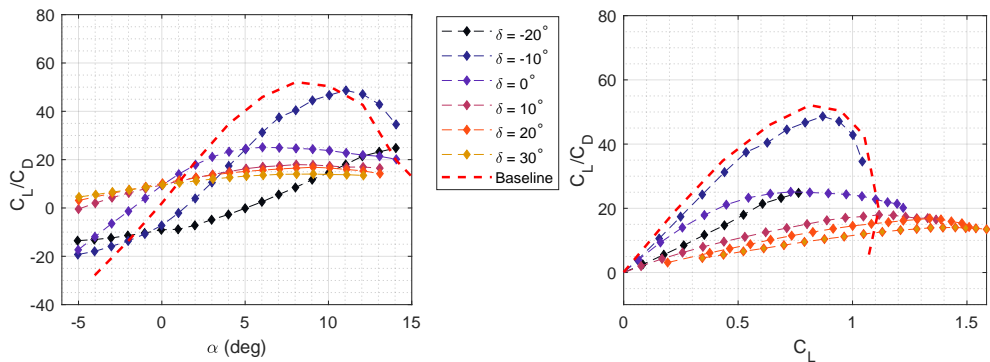

Fig. 12   Flap aerodynamic efficiency as a function of both angle of attack and lift coefficient.

To further visualize these efficiency improvements and to compare the performance of the three tested configurations, an 'efficiency envelope' that displays each configuration's best obtainable lift-to-drag ratio, as a function of achieved lift coefficient, is introduced. By doing so, the two parameters that can vary lift coefficient—angle of attack and actuation input—are condensed in a single curve that describes the best attainable performance for each configuration (Fig. 13) [32]. This condensed metric is particularly useful when comparing the aerodynamic performance of different trailing edge devices (e.g. FishBAC vs flap), as it can establish a direct comparison between different configurations that is independent of variables that may be different depending on the device—e.g. actuation inputs, camber deflections, angles of attack and flap angles.

These efficiency envelopes show that the FishBAC achieves significantly higher lift-to-drag ratios than the Flap configuration over the full range of angles of attack tested. This improved efficiency increase ranges from 160% to 27%, for low ($0° < \alpha < 5°$) and high ($\alpha > 10°$) angles of attack, respectively. Furthermore, when shown in terms of lift coefficient, the production of which is the key driver of camber change, it can be seen that the FishBAC performs better over the full range of lift coefficients achieved, and significantly better at moderate to high lift coefficients (i.e. $C_L > 0.8$), achieving an efficiency improvement of at least 200% at $C_L = 1.1 - 1.25$. For lower lift coefficients, the FishBAC has lift-to-drag ratios that are at least 16% higher than the flap's (Fig. 14).

In summary, the FishBAC is more aerodynamically efficient than the flap at all angles of attack and lift coefficients. However, the benefit of camber morphing is particularly remarkable at higher lift coefficients. The minimum efficiency improvement is of 16% at $C_L \approx 0.5$, whereas improvements above 250% are observed at higher lift coefficients. It is important to note that the FishBAC's drag measurements were performed at a 'high drag' region—i.r. near the actuation tendon, where largest camber deflections occur and tunnel wall-model interactions are more likely—whereas the Flap's drag measurements were performed at midspan, far away from the external control horns required to drive the flap and any wall effects. Lastly, it is important to note that differences between undeflected FishBAC and flap and baseline results exist. In the FishBAC's case, the $\delta = 0°$ shows higher lift than baseline NACA 23012. This is most likely due to the FishBAC having a small downward deflection, induced by either a small positive offset on the actuation input or an uneven skin tension between the top and bottom surfaces. Moreover, in the flap's case, the increased lift is potentially due to a small positive deflection angle due to an input offset. This offset is likely due to a mismatch between the actuation angle input and the flap angle. This is consistent with the higher drag results for the undeflected configuration (Fig. 9).
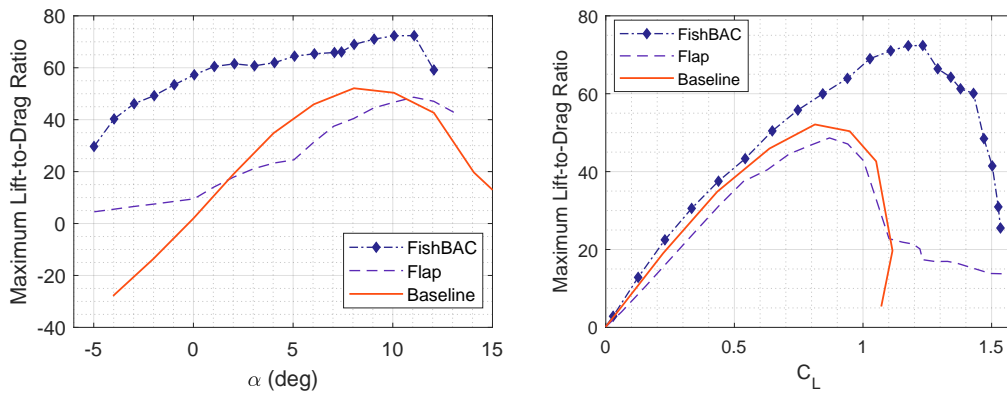

Fig. 13   Efficiency envelopes showing the best achievable lift-to-drag ratios as a function of angle of attack (left) and of lift coefficient (right).
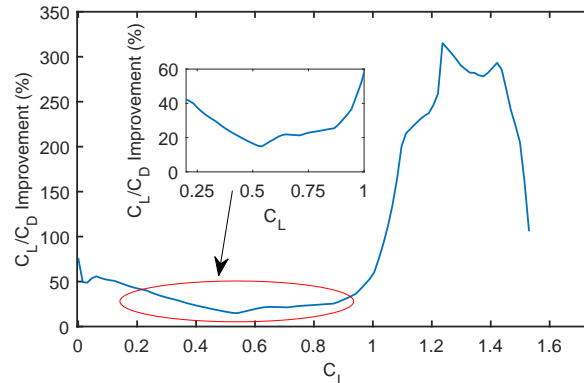

Fig. 14   Percentage improvements in FishBAC aerodynamic efficiency — compared to Flap.

13

B. Spanwise Wake Rake Drag Measurements

Wake rake survey measurements were performed at different spanwise locations to further investigate how drag varies along the span. For these measurements, both angle of attack and actuation input angle remained constant. Fig. 15 presents FishBAC's wake rake drag measurements, at a fixed angle of attack ($\alpha = 5°$) and maximum actuation input ($\delta = +40°$). The pressure ratio distributions on the top half of the wing span are only shown since the testing and actuation configuration is symmetrical. Results show a drag coefficient variation of 22% between the lowest and highest values—at midspan and at quarter-span, respectively. The wake distribution data also shows that the wake shifts down in the thicknesswise direction as the rake scans along the span, having a maximum displacement of 40 mm moving from about the midspan close to the tendon. This is likely due to variation in camber along the span due to elastic washout and/or surface imperfections. Additionally, the pressure ratio peak values and distribution are fairly uniform, with a maximum variation of less than 2.5% between the lowest and highest value. These observed differences in wake drag functions explain the relatively low variation in drag coefficients. In summary, these spanwise differences in drag coefficient and wake drag function are potentially due to elastic washout and also due to imperfections or variations in the model geometry.

Similarly, Fig. 16 shows wake rake drag measurements for the flap at several spanwise locations. Again the angle of attack was fixed at $\alpha = 5°$, but the actuation deflection input was fixed at $\delta = +20°$. The higher steadiness of the pressure data makes the $\delta = +20°$ case more suitable to be displayed as opposed to the $\delta = +30°$ case, although the lift coefficient in this case is slightly inferior compared to the FishBAC at a maximum deflection (i.e. $\delta = +40°$) presented in Fig. 15. In order to estimate the drag increase due to the presence of external actuator control horns, extra measurements were performed around their location (Fig. 15). The results show a higher variation in drag coefficient of around 55% between the lowest (at midspan) and highest (at quarter-chord) values—excluding drag coefficient measurements at the control horn. Additionally, a 466% increase in drag coefficient is observed at the control horn. This increase shows that the control horn significantly disrupts the flow and, therefore, justifies the decision to perform all Flap's drag measurements presented in Section VI.A.1 at midspan. Moreover, it is observed that near the control horn there are two separate but overlapping wake regions, perhaps due to the control horn shedding its own wake.
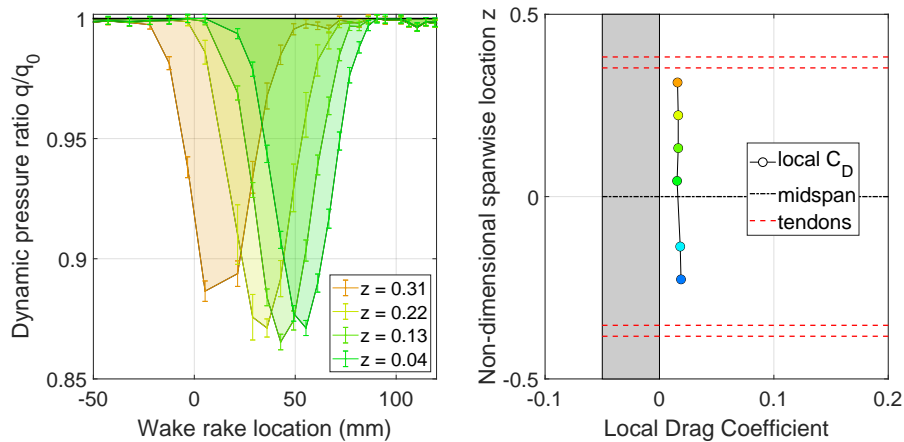

Fig. 15   FishBAC's distribution along the span of wake to free stream dynamic pressure ratio (left) and drag coefficient vs angle of attack (right) at angle of attack $\alpha = 5°$ and actuator deflection input $\delta = +40°$.
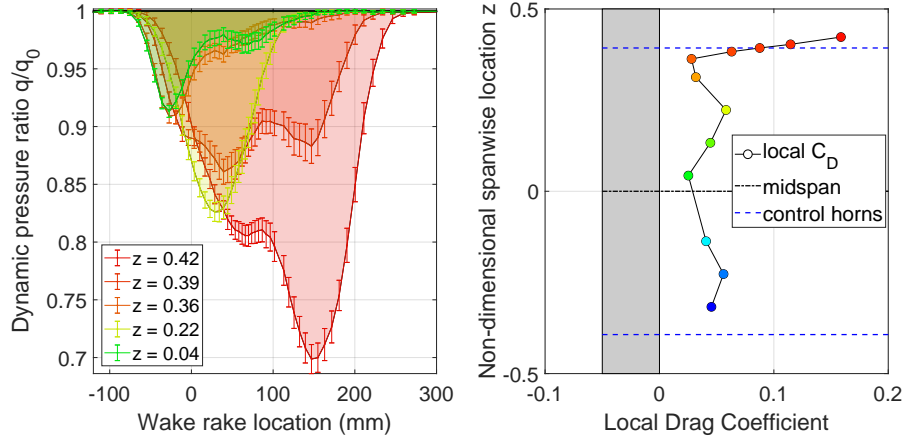
14

Fig. 16   Flap's distribution along the span of wake to free stream dynamic pressure ratio (left) and drag coefficient vs angle of attack (right) at angle of attack $\alpha = 5°$ and actuator deflection input $\delta = +20°$.

C. Particle Image Velocimetry

Particle Image Velocimetry wake measurements were performed to visualize the differences in the wakes created by the FishBAC and the flap. These results are useful to further establish the reasons for the significant improvement in performance seen with the FishBAC. These measurements were performed at four different actuation input angles: $\delta = -10°, 0°, +10°, +20°$. Fig. 17 shows images of both FishBAC and flap wakes. The wake thickness was calculated by measuring the distance, across the wake, at a distance of $0.1c$ aft of the trailing edge. The wake limits were assumed to be the points just before the flow speed becomes equal to the freestream. Wake thickness results are summarized in Table 2. Results show that the wake thickness of the FishBAC does not significantly grow with increasing deflection (over the range of δ shown here), achieving a stable value of approximately 16 mm (i.e. 6% of chord length). These results are consistent with the marginal drag increases with increasing deflection that are observed in Fig. 9. Unlike the FishBAC, the wake thickness of the flap increases significantly with deflection. For example, the wake thickness ranges from 28.59 mm to 47.02 mm (i.e. 10.5% and 17.5% of chord length), for inputs of $\delta = 0°$ and $\delta = +20°$, respectively. When compared to the FishBAC, these flap results represent an increase of between two to three times in wake thickness, which correlates to the significant higher drag shown in Section VI.A.1.

Table 2   FishBAC's and Flap's wake thickness for different actuation inputs. Results correspond to a fixed angle of attack of $\alpha = 5°$ and freestream velocity of $V = 30 \, \mathrm{m \, s^{-1}}$.

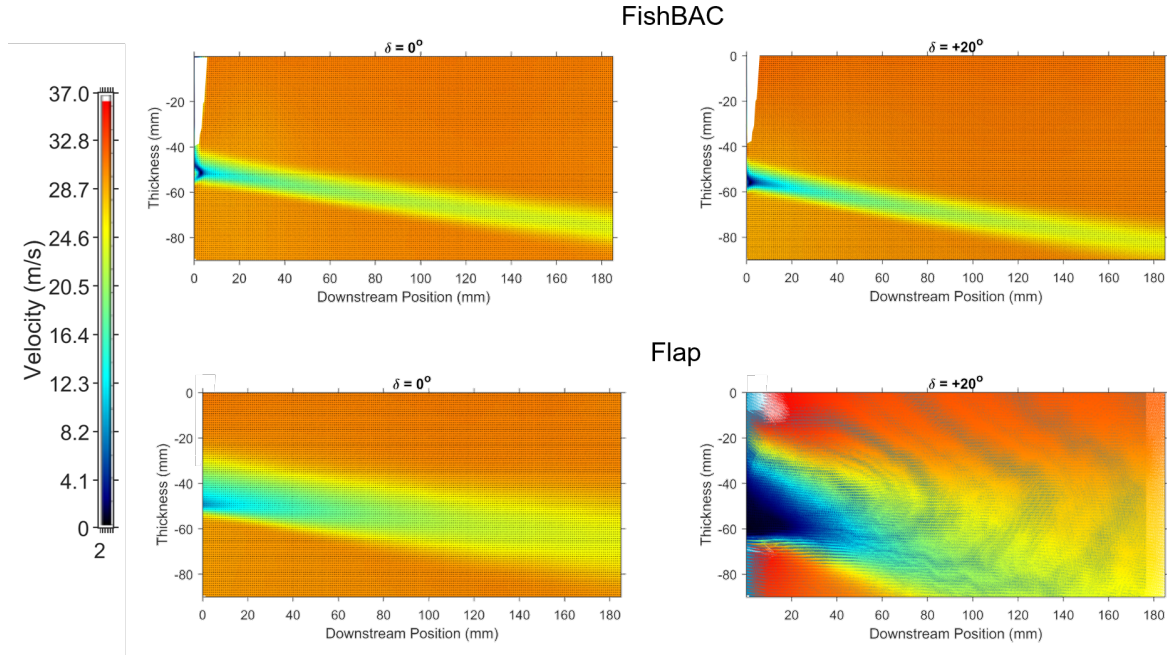| Configuration	Input Angle (deg)	Wake Thickness (mm)	Normalized Wake Thickness (t/c)
FishBAC	−10	16.08	0.0595
	0	14.65	0.0543
	+10	16.18	0.0599
	+20	16.27	0.0603
Flap	−10	29.90	0.1117
	0	28.59	0.1059
	+10	31.93	0.1183
	+20	47.02	0.1741

Fig. 17   FishBAC (top) and Flap (bottom) images obtained using 2D Particle Image Velocimetry. The measuring plane was located at the spanwise location 0.467*b*.

VII. Conclusions

An experimental wind tunnel study is performed to investigate the aerodynamic performance of the FishBAC camber morphing device and to compare it against traditional trailing edge hinged flaps. A 1-meter long NACA 23012 wind tunnel wing model was designed and manufactured to allow for testing with three different trailing edge configurations—baseline, FishBAC, and flapped. The wing was designed to span the height of Swansea University low-speed wind tunnel to create a quasi-two-dimensional flow condition. Force balance wake rake survey data were used to quantify the aerodynamic performance of the different configurations at a range of angles of attack and camber deformations at freestream velocities of 30 m/s. Additionally, optical aerodynamic measurements were performed using Particle Image Velocimetry. Consideration of the experimental data leads to the following conclusions:

1) Wind tunnel wing setup has been compared to previous experimental results presented in the literature, as well as XFOIL numeric simulations. Results show similar trends to those in the literature and XFOIL estimates, and main differences with previous experimental results are attributed to different measuring techniques—force balance and wake rake versus airfoil pressure taps.

2) The FishBAC shows a significantly higher lift-to-drag-ratio than the hinged flap. This improvement is even more remarkable at moderate to high lift coefficients (i.e. $C_L > 1$), where the improvement are at least of 50%. For lower lift coefficients, the improvement is at least 16%. In general, the FishBAC presents a higher aerodynamic efficiency than the flap, for all angles of attack and lift coefficients.

3) Wake rake results show that, for a fixed angle of attack and similar actuation input, the flap wake thickness presents significant variations, whereas the FishBAC's remains relatively stable. In terms of wake thickness, the flap shows two to four times thicker wake than the FishBAC.

4) PIV results show that the FishBAC's wake thickness is nearly constant with increasing deflection, having a stable value of 6% of chord length. Conversely, the wake thickness of the flap increases by 64% from its undeflected value, achieving a maximum wake thickness of 17.4% of chord length. Additionally, when comparing the two configurations, the flap has a wake that is two to three times the thickness of the FishBAC's wake. These results suggest that the flow is highly separated in the flap case, which is consistent with the drag increments observed in the pressure wake survey results of the hinged flap.

16

Acknowledgments

Data Access Statement

All underlying raw data used in this study are available for download from the Research Data Repository of University of Bristol, data.bris, at: `https://data.bris.ac.uk/data/dataset/1w3w5nw71enrx22zppkyd650fe`.

References

[1] Greff, E., "The development and design integration of a variable camber wing for long/medium range aircraft," *The Aeronautical Journal*, Vol. 94, No. 939, 1990, pp. 301–312.

[2] Barbarino, S., Bilgen, O., Ajaj, R. M., Friswell, M. I., and Inman, D. J., "A Review of Morphing Aircraft," *Journal of Intelligent Material Systems and Structures*, Vol. 22, No. 9, 2011, pp. 823–877. doi:10.1177/1045389X11414084.

[3] Beaverstock, C., Woods, B., Fincham, J., and Friswell, M., "Performance Comparison between Optimised Camber and Span for a Morphing Wing," *Aerospace*, Vol. 2, No. 3, 2015, pp. 524–554. doi:10.3390/aerospace2030524, URL `http://www.mdpi.com/2226-4310/2/3/524/`.

[4] Parker, H., "The Parker Variable Camber," Tech. Rep. 77, National Advisory Committee for Aeronautics, Washington, DC, 1920.

[5] Hogan, H. J., "Variable Camber Airfoil," *U.S. Patent 1,868,748*, 1932.

[6] Chilton, R., "Variable Area-and-Camber Wing," *U.S. Patent 2,222,935*, 1940.

[7] Kota, S., Hetrick, J. A., Osborn, R., Paul, D., Pendleton, E., Flick, P., and Tilmann, C., "Design and application of compliant mechanisms for morphing aircraft structures," *Proc. SPIE*, Vol. 5054, No. November, 2003, pp. 24–33. doi:10.1117/12.483869, URL `http://dx.doi.org/10.1117/12.483869`.

[8] Bilgen, O., Friswell, M. I., Kochersberger, K. B., and Inman, D. J., "Surface Actuated Variable-Camber and Variable-Twist Morphing Wings Using Piezocomposites," *Structures, Structural Dynamics and Materials Conference*, Vol. 19, No. April, 2011, pp. 1–13. doi:10.2514/6.2011-2072.

[9] Barbarino, S., Pecora, R., Lecce, L., Concilio, A., Ameduri, S., and Calvi, E., "A novel SMA-based concept for airfoil structural morphing," *Journal of Materials Engineering and Performance*, Vol. 18, No. 5-6, 2009, pp. 696–705. doi:10.1007/s11665-009-9356-3.

[10] Sofla, A., Meguid, S., Tan, K., and Yeo, W., "Shape morphing of aircraft wing: Status and challenges," *Materials & Design*, Vol. 31, No. 3, 2010, pp. 1284–1292. doi:10.1016/j.matdes.2009.09.011, URL `http://linkinghub.elsevier.com/retrieve/pii/S0261306909004968`.

[11] Diaconu, C. G., Weaver, P. M., and Mattioni, F., "Concepts for morphing airfoil sections using bi-stable laminated composite structures," *Thin-Walled Structures*, Vol. 46, No. 6, 2008, pp. 689–701. doi:10.1016/j.tws.2007.11.002.

[12] Daynes, S., Nall, S., Weaver, P., Potter, K., Margaris, P., and Mellor, P., "Bistable Composite Flap for an Airfoil," *Journal of Aircraft*, Vol. 47, No. 1, 2010, pp. 334–338. doi:10.2514/6.2009-2103, URL `http://arc.aiaa.org/doi/abs/10.2514/6.2009-2103`.

[13] Larson, R. R., "Flight Control System Development and Flight Test Experience With the F-111 Mission Adaptive Wing Aircraft," Tech. rep., NASA Ames Research Center, Edwards, California, 1986.

[14] Kudva, J. N., "Overview of the DARPA Smart Wing Project," *Journal of Intelligent Materials Systems and Structures*, Vol. 15, No. 4, 2004, pp. 261–267. doi:10.1177/1045389X04042796.

[15] Campanile, L. F., and Sachau, D., "Belt-rib concept: a structronic approach to variable camber," *Journal of Intelligent Material Systems and Structures*, Vol. 11, No. 3, 2000, pp. 215–224. doi:10.1106/6H4B-HBW3-VDJ8-NB8A.

[16] Woods, B. K. S., and Friswell, M. I., "Preliminary Investigaion of a Fishbone Active Camber Concept," *ASME Conference on Smart Materials, Adaptive Structures and Intelligent Systems*, 2012. doi:10.1017/CBO9781107415324.004.

[17] Szodruch, J., "The influence of camber variation on the aerodynamics of civil transport aircraft," *23rd Aerospace Sciences Meeting*, 1985. doi:10.2514/6.1985-353, URL http://arc.aiaa.org/doi/10.2514/6.1985-353.

[18] Szodruch, J., and Hilbig, R., "Variable wing camber for transport aircraft," *Progress in Aerospace Sciences*, Vol. 25, No. 3, 1988, pp. 297–328. doi:10.1016/0376-0421(88)90003-6.

[19] Daynes, S., and Weaver, P. M., "Morphing Blade Fluid-Structure Interaction," *53rd AIAA/ASME/ASCE/AHS/ASC Structures, Structural Dynamics and Materials Conference*, Honolulu, Hawaii, 2012. doi:10.2514/6.2012-1667.

[20] Bilgen, O., Kochersberger, K., Diggs, E., Kurdila, A., and Inman, D., "Morphing Wing Micro-Air-Vehicles via Macro-Fiber-Composite Actuators," *48th AIAA/ASME/ASCE/AHS/ASC Structures, Structural Dynamics, and Materials Conference*, 2007, pp. 1–16. doi:10.2514/6.2007-1785, URL http://arc.aiaa.org/doi/10.2514/6.2007-1785.

[21] Ai, Q., Kamliya Jawahar, H., and Azarpeyvand, M., "Experimental investigation of aerodynamic performance of airfoils fitted with morphing trailing edges," *54th AIAA Aerospace Sciences Meeting*, 2016. doi:10.2514/6.2016-1563, URL http://arc.aiaa.org/doi/10.2514/6.2016-1563.

[22] Yokozeki, T., Sugiura, A., and Hirano, Y., "Development and Wind Tunnel Test of Variable Camber Morphing Wing," *22nd AIAA/ASME/AHS Adaptive Structures Conference*, 2014, pp. 6–13. doi:10.2514/6.2014-1261, URL http://arc.aiaa.org/doi/10.2514/6.2014-1261.

[23] Woods, B. K. S., Bilgen, O., and Friswell, M. I., "Wind tunnel testing of the fish bone active camber morphing concept," *Journal of Intelligent Material Systems and Structures*, Vol. 25, No. 7, 2014, pp. 772–785. doi:10.1177/1045389X14521700.

[24] AEROTECH, A., "Operational Manual for Swansea University Low Speed Wind Tunnel," , 2017.

[25] Drela, M., "XFOIL: An Analysis and Design System for Low Reynolds Number Airfoils," *Lecture Notes in Engineering*, edited by T. Mueller, Springer, Berlin, Heidelberg, 1989, 54th ed., pp. 1–12. doi:10.1007/978-3-642-84010-4{_}1.

[26] Barlow, J., Rae, W., and Pope, A., *Low-Speed Wind Tunnel Testing*, 3rd ed., Wiley, 1999.

[27] Ashenden, R., Lindberg, W., and Marwitz, J. D., "Two-dimensional NACA 23012 airfoil performance degradation by super cooled cloud, drizzle, and rain drop icing," *34th Aerospace Sciences Meeting and Exhibition*, 1996. doi:10.2514/6.1996-870.

[28] Pouryoussefi, S. G., Mirzaei, M., Nazemi, M. M., Fouladi, M., and Doostmahmoudi, A., "Experimental study of ice accretion effects on aerodynamic performance of an NACA 23012 airfoil," *Chinese Journal of Aeronautics*, Vol. 29, No. 3, 2016, pp. 585–595. doi:10.1016/j.cja.2016.03.002, URL http://dx.doi.org/10.1016/j.cja.2016.03.002.

[29] Leishman, J. G., "Dynamic stall experiments on the NACA 23012 aerofoil," *Experiments in Fluids*, Vol. 9, 1990, pp. 49–58. doi:10.1007/s003480050014.

[30] Jacobs, E. N., and Sherman, A., "Airfoil Section Characteristics as Affected by Variations of Reynolds Number," Tech. rep., National Advisory Commitee for Aeronautics, Langley Field, Virginia, 1939.

[31] Woods, B. K. S., and Friswell, M. I., "Fluid-Structure Interaction Analysis of the Fish Bone Active Camber Mechanism," *54th AIAA/ASME/ASCE/AHS/ASC Structures, Structural Dynamics, and Materials Conference*, Boston, Massachusetts, 2013, pp. 1–15.

[32] Huntley, S. J., Allen, C. B., and Woods, B. K., "Computational Analysis of the Aerodynamics of Camber Morphing," *AIAA Aviation Forum*, Dallas, Texas, 2019, pp. 1–20. doi:10.2514/6.2019-2914.